Case Studies in Thermal Engineering 38 (2022) 102335

Contents lists available at ScienceDirect

Case Studies in Thermal Engineering

journal homepage: www.elsevier.com/locate/csite

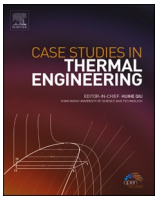

Numerical modeling of thermal runaway in high-energy lithium-ion battery packs induced by multipoint heating

Yuanmao Li [a], Guixiong Liu [a,*], Zuyu Li [b]

[a] School of Mechanical & Automotive Engineering, South China University of Technology, Guangzhou, 510641, China
[b] School of Mechanical and Mechatronic Engineering, University of Technology Sydney, Sydney, NSW, 2007, Australia

HIGHLIGHTS

- Thermal runaway in Li-ion batteries presents a safety hazard in electric vehicles.
- A numerical model was proposed combining ODEs, PDEs, CFD, and thermal radiation computations.
- A multipoint heating-based methodology was developed for the thermal abuse test.
- Natural convection and thermal radiation affected the time and peak temperatures of thermal runaway.
- Cell-to-cell gaps affected thermal propagation characteristics at the pack level.

ARTICLE INFO

Keywords:
Thermal runaway
Thermal abuse
High-energy lithium-ion battery pack
Multipoint heating

ABSTRACT

Thermal runaway in lithium-ion batteries is a primary safety concern in electric vehicles (EVs). Herein, a numerical thermal abuse model is proposed that integrates ordinary differential equations (ODEs), heat-transfer partial differential equations (PDEs), natural convection in computational fluid dynamics (CFD), and thermal radiation to investigate thermal propagation in a battery pack. A three-dimensional geometric model of a high-energy lithium-ion battery pack comprising 18,650 format cells was constructed to analyze the thermal characteristics using the finite element method (FEM). A thermal abuse test was conducted to simulate the spread of thermal runaway in cells owing to multipoint heating. The maximum differences in the peak temperature between the proposed model and the model without convection were −150 K and 52.0 s, respectively, while the differences between the proposed model and the model without radiation were −52.4 K and −125.0 s, respectively. Furthermore, four additional models with different cell-to-cell gaps were constructed to study the thermal propagation characteristics, showing that the presence of a cell-to-cell gap accelerated heat transfer but compromised energy density for the battery pack. Ultimately, the coupling model at the pack level proposed in this study can improve the design of battery thermal management systems.

1. Introduction

Rapid developments have occurred in the field of EVs in recent years. Ternary lithium-ion batteries are widely used in these vehicles owing to their high energy density, voltage plateau, and excellent rate performance [1–3]. However, spontaneous combustion and explosions induced by thermal runaway in lithium-ion batteries are primary safety concerns in EVs [4–6]. Thermal runaway is a phenomenon in which an exothermic chain reaction induces an uncontrollable increase in the temperature of a cell. This can be caused

* Corresponding author.
E-mail address: megxliu@scut.edu.cn (G. Liu).

https://doi.org/10.1016/j.csite.2022.102335
Received 10 January 2022; Received in revised form 12 April 2022; Accepted 30 July 2022
Available online 7 August 2022

by mechanical, electrical, or thermal factors or a combination thereof [7–11]. When thermal runaway occurs in a single battery cell, the conduction of heat to peripheral cells via thermal diffusion results in a chain reaction, inducing thermal runaway in cells throughout the battery pack [12]. Therefore, extensive studies on the characteristics of thermal propagation in battery packs are essential for mitigating this crisis.

To evaluate the safety performance of EVs, abuse tests are typically performed to induce thermal runaway in a battery pack [13]. Standards for abuse tests have been proposed by different nations and organizations, such as the Chinese standard, GB, and the American standards belonging to the Society of Automotive Engineers (SAE), Underwriter Laboratories (UL), and International Electrotechnical Commission (IEC) series. Several methods for triggering thermal runaway have also been recommended, such as partial heating, nail penetration, and overcharging [14–17]. Among these, partial heating is the easiest method to implement in battery packs. Thermal runaway characteristics have been extensively studied using numerical simulations and experiments [18–21]. Lopez et al. [22] characterized exothermic side reactions using a thermal abuse model that was validated during a constant-power heating test. They demonstrated the effects of convection conditions, physical cell configurations, and electrolyte combustion on the thermal behavior of the cell. Shah et al. [23] derived and experimentally validated a nondimensional parameter to predict thermal runaway in cells. They also identified safe and unsafe regions in thermal design spaces, thereby improving thermal management design. Zhao et al. [24] considered five side reactions to establish a thermal abuse model and analyzed the thermal characteristics of separators, such as the heating temperature, dissipation coefficient, heating area, and temperature distribution, under varying operational conditions. An et al. [25] developed and experimentally validated an electrochemical-thermal simulation model. Their proposed model was used to study the effects of key parameters and thermal properties of thermal runaway induced by ultrahigh discharge rates. They also proposed an effective thermal runaway prevention strategy based on the transfer of boiling heat via miniature channels. Kong et al. [26] developed a 3D abuse model under local heating conditions and analyzed the effects of various battery materials, external heating conditions, and heat dissipation on thermal runaway. Their results indicated that heating near the bottom of the cells is more likely to induce thermal runaway than heating at other positions.

Thermal abuse tests are typically performed at the vehicle level; however, these are numerically difficult to implement. Testing at smaller levels is more efficient, with the pack level preferable to the cell or module levels as thermal propagation is strongly influenced by the grouping configurations within packs. A review of the related literature reveals that thermal runaway behavior has rarely been researched at the pack level, especially when the rated energy exceeds 1000 Wh [27–29], as considered in this study. Moreover, despite the fact that accidents in EVs such as overheating, short circuits, overcharging, and crashes, are typically caused by thermal runaway in multiple cells, most existing research on the thermal propagation characteristics of batteries has focused on single cells. In this context, our investigation into the thermal propagation behavior induced by thermal runaway in multiple cells in high-energy lithium-ion battery packs is expected to be of great significance for the future design of thermal management systems.

In this study, an abuse model was proposed by considering four main exothermic side reactions to simulate the pack-level thermal runaway behavior induced by multipoint heating. A high-energy pack was used for the simulation of the thermal abuse model, comprising a group of 192 NMC811 battery cells in 18,650 format with a total rated energy of 2073.6 Wh. The nominal capacity and voltage of each cell was 3000mAh@1C and 3.6 V, respectively. The battery pack consisted of four modules, each comprising 48 cells. Natural convection and thermal radiation, which influence thermal propagation within a pack, were coupled with the thermal abuse model to enhance the accuracy. Subsequently, a numerical model was developed by combining the thermal runaway ODEs, heat conduction PDEs, natural convection in CFD computations, and radioactive heat-transfer equations. Finally, the results obtained using the finite element method (FEM) during the simulation were discussed. The objectives of our study were as follows:

To build a numerical model combining ODEs, PDEs, CFD, and thermal radiation computations.

To simulate thermal runaway in a high-energy lithium-ion battery pack induced by multipoint heating, using the finite element method (FEM).

To discuss the effects of natural convection and thermal radiation on thermal propagation characteristics at the pack level.

To discuss the effects of the cell-to-cell gap on thermal runaway behavior and suggest a prevention strategy to mitigate safety crises based on thermal management systems.

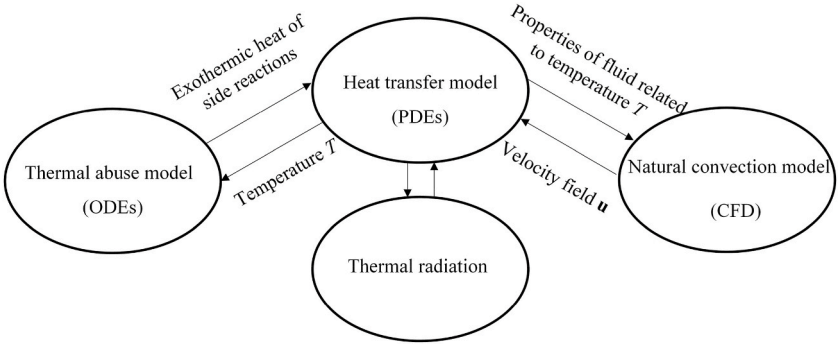

Fig. 1. Schematic of the coupling relationships in model development.

2. Materials and methods

As aerial convection and thermal radiation influence the characteristics of thermal propagation in packs, natural convection was considered in combination with heat transfer when constructing the thermal abuse model proposed in this study. The thermal abuse model comprised ODEs with four exothermic side reactions and the solid heat-transfer model was described using PDEs. Furthermore, the natural convection model was based on CFD. Thus, the model proposed in this study combined ODEs, PDEs, CFD, and thermal radiation computations. The relationships between these components are illustrated in Fig. 1. ODEs were used to calculate the heat of the side reactions induced by thermal runaway in packs at different critical temperatures. Simultaneously, PDEs considered ODEs as the heat sources in cells. Moreover, the temperature, T, calculated using the PDEs was used to determine the side reaction and exothermic heat in the ODEs. It is known that the velocity field in CFD affects the value of T in PDEs. However, some of the fluid properties obtained using CFD are functions related to T. As the cells will reach very high temperatures, radiative heat transfer is expected to be an important mode. Hence, to improve the accuracy of the proposed model, the thermal radiation aspect of energy dissipation was also considered. Further details are provided in subsequent sections.

2.1. Thermal abuse model

Four side reactions were considered in the abuse model: the decomposition of SEI; the reaction between the negative electrode and the electrolyte; the reaction between the positive electrode and the electrolyte; and the decomposition of the electrolyte. The abuse model can be described using Arrhenius kinetics [30–33], and the total exothermic heat generation rate $q_{\text{ele-chem}}$ for thermal runaway was calculated as follows:

$$q_{ele-chem} = q_{\text{sei}} + q_{\text{ne}} + q_{\text{pe}} + q_{\text{e}}. \tag{1}$$

2.1.1. Decomposition of SEI

When the temperature of the cell exceeded 363.15 K, the SEI film decomposed via an exothermic reaction. In the equations below, H_{sei} is used to denote the heat released per kilogram of the decomposed SEI film; W_{c} denotes the unit carbon content (the proportion of carbon per unit volume) before thermal runaway; A_{sei} denotes the decomposition frequency factor of the SEI film, which depends on the conductivities of the two electrodes of the battery; $E_{\text{a,sei}}$ denotes the activation energy of the decomposition reaction; C_{sei} denotes the carbon content in the SEI film; and m_{sei} denotes the reaction order. Thus, the heat generation rate, q_{sei}, of the decomposition of the SEI film is given by:

$$q_{\text{sei}} = H_{\text{sei}} W_{\text{c}} R_{\text{sei}} \tag{2}$$

$$R_{\text{sei}}(T, C_{\text{sei}}) = A_{\text{sei}} \exp(-\frac{E_{\text{a,sei}}}{RT}) C_{\text{sei}}^{m_{\text{sei}}} \tag{3}$$

$$R_{\text{sei}} = -\frac{dC_{\text{sei}}}{dt} \tag{4}$$

2.1.2. Reaction between the negative electrode and the electrolyte

When the temperature of the cell exceeded 393.15 K, an exothermic reaction was initiated between the negative electrode and the electrolyte. In this section, H_{ne} is used to denote the exothermic heat released per kilogram of the negative electrode; W_{c} denotes the unit carbon content; A_{ne} and $E_{\text{a,ne}}$ denote the frequency factor and activation energy, respectively, of the reaction between the negative electrode and the electrolyte; t_{sei} denotes the dimensionless thickness of the SEI film; C_{ne} denotes the carbon content of lithium; and m_{ne} denotes the reaction order. The heat generation rate, q_{ne}, of the reaction between the negative electrode and electrolyte is given by:

$$q_{\text{ne}} = H_{\text{ne}} W_{\text{c}} R_{\text{ne}} \tag{5}$$

$$R_{\text{ne}}(T, C_{\text{ne}}, t_{\text{sei}}) = A_{\text{ne}} C_{\text{ne}}^{m_{\text{ne}}} \exp(-\frac{E_{\text{a,ne}}}{RT} - \frac{t_{\text{sei}}}{t_{\text{seio}}}) \tag{6}$$

$$R_{\text{ne}} = \frac{dt_{\text{sei}}}{dt} = -\frac{dC_{\text{ne}}}{dt} \tag{7}$$

2.1.3. Reaction between the positive electrode and the electrolyte

When the temperature of the cell exceeded 443.15 K, an exothermic reaction was initiated between the positive electrode and electrolyte. Here, H_{pe} is used to denote the heat generated per kilogram of the positive electrode and the electrolyte, W_{p} denotes the unit carbon content, A_{pe} denotes the frequency factor of the reaction between the negative electrode and the electrolyte, $E_{\text{a,pe}}$ denotes the activation energy of the reaction between the negative electrode and the electrolyte, α denotes the conversion degree of the positive electrode material, and m_{pe} denotes the reaction order. The heat generation rate, q_{pe}, of the reaction between the positive electrode and electrolyte is given by:

$$q_{\text{pe}} = H_{\text{pe}} W_{\text{p}} R_{\text{pe}}, \tag{8}$$

$$R_{\text{pe}}(T, \alpha) = A_{\text{pe}} \alpha^{m_{\text{pe}}} (1-\alpha)^{m_{\text{pe}}} \exp(-\frac{E_{\text{a,pe}}}{RT}) \tag{9}$$

$$R_{pe} = \frac{d\alpha}{dt}. \tag{10}$$

2.1.4. Decomposition of the electrolyte

When the cell temperature exceeded 473.15 K, the electrolyte began to decompose. H_e is used to denote the heat generated by the decomposition of each kilogram of the electrolyte; W_e denotes the unit carbon content of the electrolyte; A_e, $E_{a,e}$, and C_e denote the frequency factor of electrolytic decomposition, activation energy of electrolytic decomposition, and proportion of the remaining electrolyte, respectively; and m_e denotes the reaction order. The heat generation rate, q_e, of electrolytic decomposition is given by:

$$q_e = H_e W_e R_e, \tag{11}$$

$$R_e(T, C_e) = A_e \exp(-\frac{E_{a,e}}{RT}) C_e^{m_e}, \tag{12}$$

$$R_e = -\frac{dC_e}{dt}. \tag{13}$$

The ambient temperature was set to 293.15 K, and the kinetic parameters that were used for each electrochemical reaction in the abuse model (in a fully charged cell) are summarized in Table 1 [22].

As described in the preceding sections, discrete changes can be observed in the exothermic heat release when the cells cross certain critical temperatures. This is equivalent to multiplying the heat generation rate by a step function at each critical point during the model development. However, this interferes with the convergence of the model when using the FEM. To mitigate this problem, an effective solution was proposed to smoothen the step function, which significantly increased the solution speed of the model. The acceptable margin of error for temperature was assumed to be 3 K because the side reactions do not immediately release a large amount of heat after crossing the critical temperatures; instead, a temperature transition zone of 3 K was observed. Furthermore, to enhance its applicability for modeling, a second-order continuous differentiable smoothed function was selected. Hence, the smoothed function replaced the aforementioned step function in the model and was defined as follows:

$$f_{smooth}(x) = \begin{cases} 0, x < 0 \\ 2x^5/81 - 5x^4/27 + 10x^3/27, 0 \le x \le 3. \\ 1, x > 3 \end{cases} \tag{14}$$

The schematic of smoothed function is illustrated in Fig. 2. The green part was the transition zone.

For example, when the cell temperature reaches 363.15 K, the SEI begins to decompose via an exothermic reaction that produced a large amount of heat in an instant. However, in the developed numerical model, the heat, q_{sei}, is added directly to the solid heat-transfer model as an external heat source. This means that sudden changes will occur in the heat-transfer PDEs at the critical temperatures of 363.15 K, 393.15 K, 443.15 K, and 473.15 K. Hence, the reaction rate of x, R_x, in Eq. (3), Eq. (4), Eq. (6), Eq. (7), Eq. (9), Eq. (10), Eq. (12), and Eq. (13) can be revised as:

$$R_{x,revise} = R_x \cdot f_{smooth}(T - T_x) \tag{15}$$

where x = {sei, ne, pe, e}; T denotes the temperature of the cell; T_x denotes the critical temperatures of x.

2.2. Transient heat-transfer governing model

The transient heat-transfer governing model was coupled with the thermal abuse model, and considered solid heat-transfer PDEs, natural convection in CFD, and thermal radiation computations. This model can be described as follows:

$$\rho C_p \frac{\partial T}{\partial t} + \rho C_p \mathbf{u} \cdot \nabla T + \nabla \cdot (\mathbf{q}_c + \mathbf{q}_r) = Q + Q_p + Q_{vd} \tag{16}$$

where $\rho C_p \frac{\partial T}{\partial t}$ denotes the time-accumulation term in both solid heat-transfer PDEs and CFD; ρ, C_p, and T denote the density, heat capacity, and temperature, respectively; $\rho C_p \mathbf{u} \cdot \nabla T$ denotes the convection term; $\mathbf{u}$ denotes the velocity field of the fluid, which is given by CFD computations; $\mathbf{q}_c$ includes the solid and fluid conduction heat transfer ($\mathbf{q}_{c,s}$, $\mathbf{q}_{c,f}$); $\mathbf{q}_r$ denotes thermal radiation; Q denotes the term arising from external heat sources, including the electrochemical reaction heat in the thermal abuse model and the external heat source of the heater mentioned in section 3; and Q_p and Q_{vd} denote the terms of pressure work and viscous dissipation, respectively, in CFD.

Table 1
Kinetic parameters for the exothermic reaction of the thermal abuse model.

x	H_x/J·kg^{-1}	W_x/kg·m^{-3}	A_x/s^{-1}	$E_{a,x}$/J·mol^{-1}	C_x/1	m_x/1
sei	2.57×10^5	$W_c = 1390$	1.667×10^{15}	1.3508×10^5	0.15	1
ne	1.714×10^6		2.5×10^{13}	1.3508×10^5	0.75, $t_{sei} = 0.033$	1
pe	3.14×10^5	1300	6.67×10^{13}	1.396×10^5	$\alpha = 0.04$	1
e	1.55×10^5	500	5.14×10^{25}	2.74×10^5	1	1

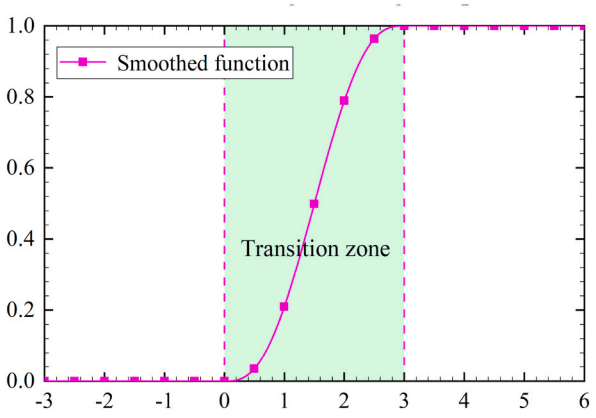

Fig. 2. Schematic of smoothed function.

2.2.1. Heat-transfer model

The solid components considered in this study primarily included diaphragms and the 192 battery cells used in the battery packs. In addition to the time-accumulation term described in Eq. (16), the heat-transfer model included the solid conduction heat transfer, which can be expressed as:

$$\mathbf{q}_{\mathrm{c,s}} = -k_{\mathrm{s}}\nabla T \tag{17}$$

where k_{s} denotes solid thermal conductivity coefficient.

Because the structure of a cell is assumed to be cylindrical in the heat-transfer model, its thermal conductivity coefficient is particularly important. As a result, cylindrical coordinate systems were considered for all 192 cells, where the center of the bottom surface of each cell was considered the origin. In the cylindrical coordinate system, the radial thermal conductivity coefficient of the cell, $k_{\mathrm{cell\_r}}$, is given by the following equation [32,34]:

$$k_{\mathrm{cell\_r}} = \frac{\sum_i L_i + \sum_j L_j}{\sum_i L_i/k_i + \sum_j L_j/(\varepsilon_j \cdot k_{ele} + (1-\varepsilon_j)\cdot k_j)} \tag{18}$$

The thermal conductivity coefficient in angular direction, $k_{\mathrm{cell\_ang}}$, and in z-axis direction, $k_{\mathrm{cell\_z}}$, of the cell are given by Eq. (19) [32]:

$$k_{\mathrm{cell\_ang}} = k_{\mathrm{cell\_z}} = \frac{\sum_i L_i \cdot k_i + \sum_j L_j \cdot (\varepsilon_j \cdot k_{ele} + (1-\varepsilon_j)\cdot k_j)}{\sum_i L_i + \sum_j L_j} \tag{19}$$

The density of the cell is given by:

$$\rho_{\mathrm{cell}} = \frac{\sum_i L_i \cdot \rho_i + \sum_j L_j \cdot (\varepsilon_j \cdot \rho_{ele} + (1-\varepsilon_j)\cdot \rho_j)}{\sum_i L_i + \sum_j L_j} \tag{20}$$

And finally, the heat capacity of the cell is given by:

$$C_{\mathrm{cell}} = \frac{\sum_i L_i \cdot C_i + \sum_j L_j \cdot (\varepsilon_j \cdot C_{ele} + (1-\varepsilon_j)\cdot C_j)}{\sum_i L_i + \sum_j L_j} \tag{21}$$

In the above Eq. 18–21, i = {pos_cc, neg_cc}, j = {pos, neg, sep}.The descriptions and values of the physical properties of the thermal parameters of the battery are listed in Table 2 [35–37]. L_x, k_x, ρ_x, C_x, and ε_x denote the length, thermal conductivity coefficient,

Table 2
Descriptions and values of the physical properties of the thermal parameters of the battery.

x	L_x/m	k_x/W·m^{-1}·K^{-1}	ρ_x/kg·m^{-3}	C_x/J·kg^{-1}·K^{-1}	ε_x	Description
cell	1.42×10^{-4}	$k_{\mathrm{cell\_r}} = 0.86901$, $k_{\mathrm{cell\_ang}} = k_{\mathrm{cell\_z}} = 28.034$	2193.9	1234.4	NA	battery cell
pos	4×10^{-5}	3.4	2500	1000	0.29	positive electrode
neg	6×10^{-5}	1.04	2600	1437.4	0.31	negative electrode
pos_cc	6×10^{-6}	238	2700	903	NA	positive current collector
neg_cc	6×10^{-6}	398	8900	385	NA	negative current collector
sep	3×10^{-5}	0.344	492	1973	0.4	separator
ele	NA	0.45	1290	1046	NA	electrolyte

NA: not available.

density, heat capacity, and electrolyte phase volume fraction of x, respectively.

2.2.2. Natural convection model

Thermal propagation plays a critical role in the thermal analysis of battery packs. However, most existing studies have focused on the aerial conduction of heat, and the inclusion of the natural convection model is expected to improve the thermal propagation model. The natural convection model was constructed using equations for the conservation of energy, momentum, and mass. The equation for the conservation of energy was described using the heat-transfer equation with a convection term. As shown in Eq. (16), this was integrated into a total energy equation with the solid heat transfer and thermal radiation governing equations. Additionally, the fluid conduction heat transfer, $\mathbf{q}_{c,f}$, is given by:

$$\mathbf{q}_{c,f} = -k_f \nabla T \tag{22}$$

where k_f denotes the fluid thermal conductivity coefficient.

The Navier–Stokes equation for the conservation of momentum is as follows:

$$\rho_f \frac{\partial \mathbf{u}_f}{\partial t} + \rho_f(\mathbf{u}_f \cdot \nabla)\mathbf{u}_f = -\nabla P + \rho_f g + \mu \nabla^2 \mathbf{u}_f, \tag{23}$$

where $\rho_f \frac{\partial \mathbf{u}_f}{\partial t}$ denotes the change in velocity with time, $\rho_f(\mathbf{u}_f \cdot \nabla)\mathbf{u}_f$ denotes the convective term, $-\nabla P$ denotes the pressure gradient of fluid flows, $\rho_f g$ denotes the external gravitational force on the fluid, and $\mu\nabla^2\mathbf{u}_f$ denotes the velocity diffusion determined by viscosity, μ.

Moreover, the rate of mass reduction in the control body should be equal to the net outflow of mass. Therefore, the continuity equation for mass conservation can be expressed as:

$$\frac{\partial \rho_f}{\partial t} + \nabla \cdot (\rho_f \mathbf{u}_f) = 0 \tag{24}$$

Finally, the temperature, T, is crucial to ensure a double-sided, strong coupling between the thermal abuse, solid heat transfer, and natural convection models. In the coupled model, air was the only fluid. As a result, the physical properties of air, such as ρ_f, $C_{p,f}$, k_f, and μ, are functions of the temperature [38]. The fluid density is given by:

$$\rho_f = \frac{0.02897 p_A}{RT} \tag{25}$$

where p_A denotes the absolute pressure, and R denotes the molar gas constant, equal to 8.314472 J/(mol·K).

Moreover, $C_{p,f}$ (J·kg^{-1}·K^{-1}), k_f (W·m^{-1}·K^{-1}), and μ (Pa·s) can be expressed using the fourth-order polynomials of T (K) as follows [38]:

$$\begin{aligned} &C_{p,f} = a_{0,C} + a_{1,C}T + a_{2,C}T^2 + a_{3,C}T^3 + a_{4,C}T^4 \quad 200 \le T \le 1600 \\ &1004.6495 \le C_{p,f} \le \quad 1246.7283, \end{aligned} \tag{26}$$

$$\begin{aligned} &k_f = a_{0,k} + a_{1,k}T + a_{2,k}T^2 + a_{3,k}T^3 + a_{4,k}T^4 \quad 200 \le T \le 1600 \\ &0.0180 \le k_f \le \quad 0.1001, \end{aligned} \tag{27}$$

$$\begin{aligned} &\mu = a_{0,\mu} + a_{1,\mu}T + a_{2,\mu}T^2 + a_{3,\mu}T^3 + a_{4,\mu}T^4 \quad 200 \le T \le 1600 \\ &1.3153 \times 10^{-5} \le \mu \le 5.6258 \times 10^{-5}, \end{aligned} \tag{28}$$

The polynomial coefficients are listed in Table 3.

2.2.3. Thermal radiation

The thermal radiation component of energy dissipation was considered in the proposed model:

$$q_r = \varepsilon\sigma(T^4 - T_{amb}^4) \tag{29}$$

where the emissivity ε of the cell and diaphragms are 0.8 and 0.87, respectively [24,39], σ is the Stefan-Boltzmann constant, and T_{amb} is the ambient temperature.

Table 3
Values of the coefficients in the polynomial expressions for C_p, f, and k_f.

x	$a_{0,x}$	$a_{1,x}$	$a_{2,x}$	$a_{3,x}$	$a_{4,x}$
C	1047.63657	−0.372589265	$9.45304214 \times 10^{-4}$	$-6.02409443 \times 10^{-7}$	$1.2858961 \times 10^{-10}$
k	−0.00227583562	$1.15480022 \times 10^{-4}$	$-7.90252856 \times 10^{-8}$	$4.11702505 \times 10^{-11}$	$-7.43864331 \times 10^{-15}$
μ	-8.38278×10^{-7}	$8.35717342 \times 10^{-8}$	$-7.69429583 \times 10^{-11}$	$4.6437266 \times 10^{-14}$	$-1.06585607 \times 10^{-17}$

2.3. 3D model of the battery pack

To simulate the thermal runaway in high-energy packs, a 3D geometric model of a pack was constructed, comprising 192 NMC811 battery cells in 18,650 format. For ease of calculation, the cell structure was assumed to be cylindrical. Three heated points were randomly selected for the thermal abuse test. Fig. 3 shows a schematic of the 3D geometric model. The pack comprised of four modules, each containing 48 cells and 2 diaphragms. The cell-to-cell gap in the pack was filled with air. The cells were numbered from 1# – 48# in each module, with the notation A1# denoting the first cell in module A. The pack was completely encased in a metal enclosure of 2 mm thickness, as this thin shell structure can be set directly to avoid the difficulty of geometric modeling and meshing. Cells A24#, C23#, and D1# were randomly selected as heating points. In the thermal abuse test, heating units were used to replace selected cells and no exothermic side reactions were observed in these units.

The mesh model of the pack is illustrated in Fig. 4. Because the exothermic side reactions of the cells play the most important role in thermal analysis, the meshing of the cells must be carefully selected. Consequently, the cells were divided into smaller elements to achieve a higher calculation accuracy. In the aggregate, 1090504 elements and 186,028 nodes were considered in the FEM.

3. Numerical simulations

The simulation experiment for the thermal abuse test is described in this section. All cells in the pack were simulated at 100% state of charge. Therefore, the kinetic parameters for the exothermic reactions of the abuse model in a fully charged cell were used (refer to Table 1). Heating at the three randomly selected points (cells A24#, C23#, and D1#) induced thermal runaway in the cells of the pack. A total heating power of at least 600 W is recommended by the Chinese standard, GB 38031–2020, when the rated energy of the pack exceeds 800 Wh. In contrast, the American standard SAE J2464-2009 suggests that the external heating source should induce thermal runaway in the cell within 5 min. Therefore, a total heating power of 600 W was used during the abuse test with 200 W at each heating point. The simulation results corroborated that the first cell near each heating location entered thermal runaway within 5 min of heat application in section 4.1. The choice of heating power satisfied the requirements of the SAE standard. In this simulation test, heating units were used to replace the heating cells, with no side reactions at the heating locations. Furthermore, each heating unit continued to supply heat until the temperature of any one of the neighboring cells reached 573.15 K.

Multipoint heating was used to simulate thermal abuse in a high-energy pack. In the proposed model, the thermal abuse model described by the ODEs was coupled with heat conduction PDEs, natural convection in CFD, and thermal radiation computations. The negative *y*-axis was taken as the direction of gravity in aerial convection, depicted in Fig. 2. Natural convection was considered when defining the boundary conditions of the pack. However, instead of coupling external natural convection with CFD, convective heat flux was used, which is equivalent to heat conduction [40]. This was done to simplify the geometric and meshing models. The no-slip boundary condition was selected for the wall node; that is, the viscosity of air at the fluid-solid junction was considered. Finally, the variations in the temperature and electrochemical parameters of each cell were recorded to study thermal propagation at the pack level. Finite element analysis [41] was performed using the COMSOL Multiphysics software. The computation time of the proposed model using the Jupiter cluster of UTS iHPC (2 x AMD EPYC 7532, 32 cores, 2.40 GHz CPU, 512 GB RAM, and Red Hat Enterprise Linux 7.9) was 122 h 21 min 33 s, while those of the model without natural convection and without thermal radiation were 68 h 16 min 59 s and 56 h 1 min 55 s, respectively.

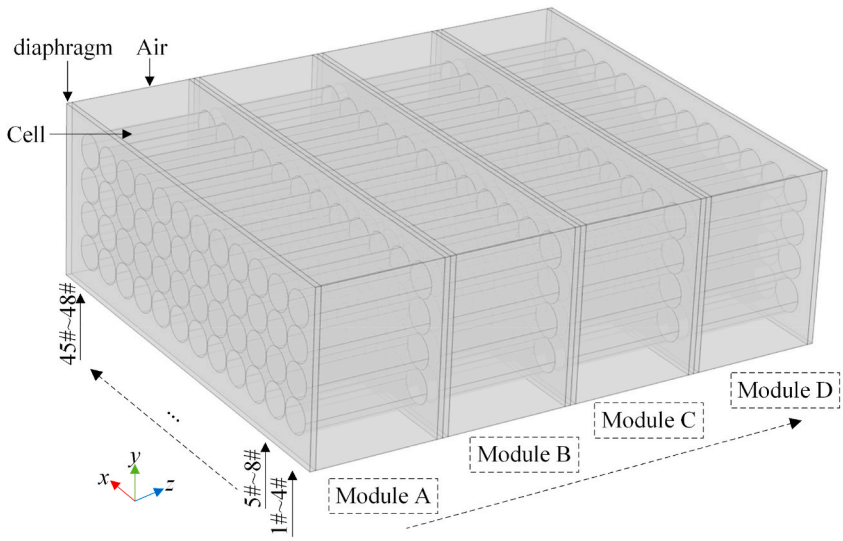

Fig. 3. Schematic of the 3D geometric model of the pack level.

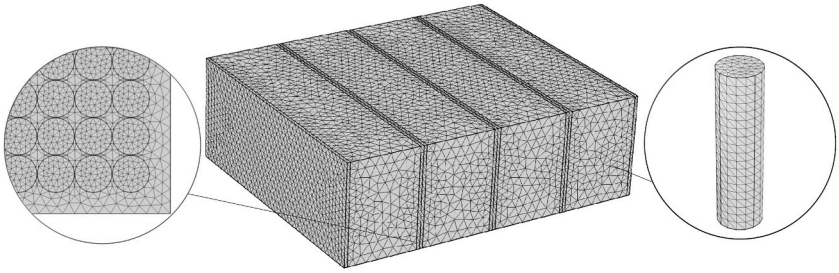

Fig. 4. Schematic of the meshing of the pack.

4. Results and discussion

In this study, a numerical model with a gap width of 0 mm combining ODEs, PDEs, CFD, and thermal radiation computations was simulated using the FEM. During the simulation, thermal runaway was induced in a high-energy lithium-ion battery pack via multipoint heating. Simultaneously, two additional simulation models were run, neglecting either natural convection or thermal radiation. Thus, the effects of natural convection and thermal radiation were investigated, confirming whether these significantly affected the performance of the proposed model. Furthermore, models were constructed to analyze the effect of the cell-to-cell gap on thermal runaway behavior in the proposed framework, considering gaps of 1, 2, 3, and 4 mm. Further details regarding thermal propagation in the battery packs are presented and discussed in this section.

4.1. *Effect of natural convection and thermal radiation*

The uncontrollable increase in the temperature of a cell observed during thermal runaway is induced by an exothermic chain reaction [42,43]. This typically corresponds to inflection points in the temperature curve of the cell, leading to a rapid increase. It was observed that all cells in the pack entered thermal runaway during the simulation using the proposed model, as well as those using the models without natural convection or thermal radiation. The cells adjacent to the heaters in each module were the first to enter thermal runaway and generated a large amount of heat, causing the temperature of other cells to rise. When the other cells reached the critical

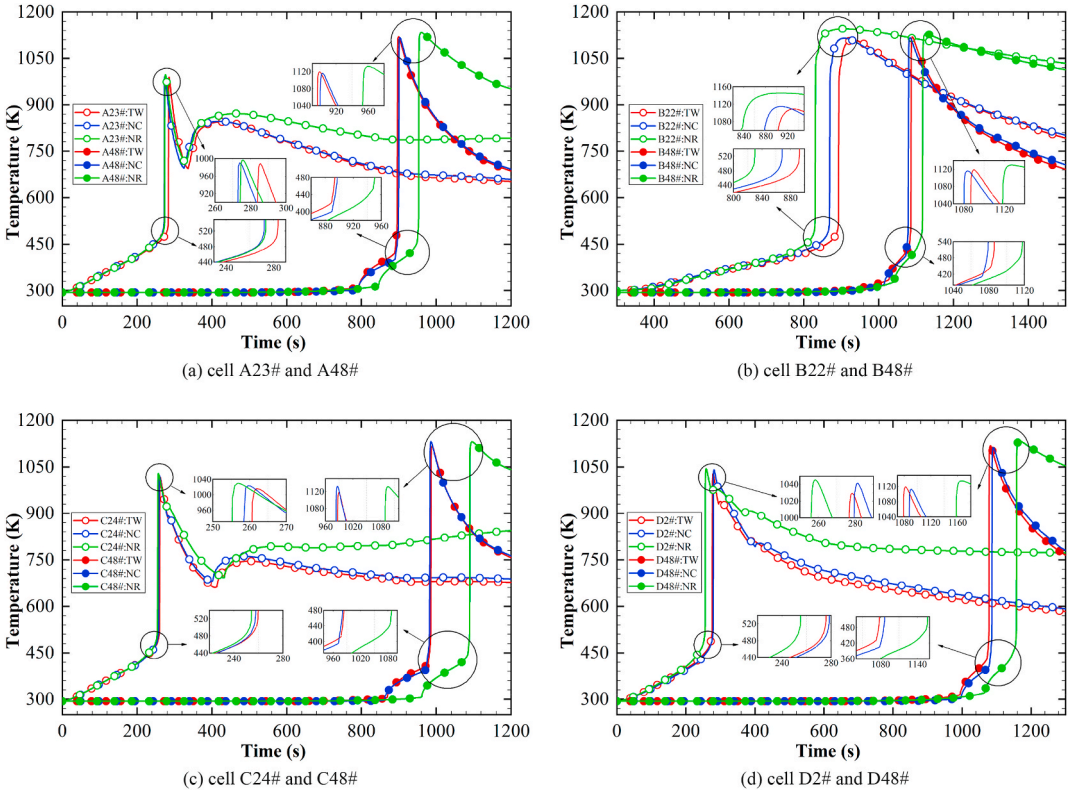

(a) cell A23# and A48#

(b) cell B22# and B48#

(c) cell C24# and C48#

(d) cell D2# and D48#

Fig. 5. Variations in the average temperatures of the cells in the three models: (a) cell A23# and A48#, (b) cell B22# and B48#, (c) cell C24# and C48#, and (d) cell D2# and D48#. Note: this work (TW) denotes the model presented in this work, no convection (NC) denotes the model without convection, and no radiation (NR) denotes the model without radiation.

temperature, they also entered thermal runaway, and this eventually spread to the entire pack. In the model proposed in this study, A23#, B22#, C24#, and D2# were the first cells in each module to enter thermal runaway, while A48#, B48#, C48#, and D48# were the last cells. It seemed that natural convection did not change the sequence of the first and last cells entering thermal runaway. This may have been because there was no airflow, as the cell-to-cell gap was 0 mm in these simulations. However, when the influence of thermal radiation was neglected, the first cell to enter thermal runaway in module B was slightly different, observed to be B21#. Furthermore, the last cells entering the thermal runaway in modules B and C were observed to be B45# and D45#, respectively.

Because the first and last cells entering thermal runaway play a vital role in the thermal propagation characteristic, the variations in the average temperatures of these cells (observed for the proposed model) are of interest (Fig. 5). Initially, thermal propagation appeared to be primarily based on heat conduction and thermal radiation, as the first cells to enter thermal runaway in all three modules were adjacent to the respective heaters. Therefore, there was no significant difference in the time taken by cells A23#, C24#, and D2# to enter thermal runaway. During the short period of thermal runaway, the temperature increased owing to the exothermic side reactions of the cell. When the exothermic side reactions were completed, the temperature of the cell started to decrease owing to the outward conduction, convection, and radiation of heat. However, after reaching the peak value, the temperature decreased more quickly in the full model proposed in this study, compared with the models neglecting natural convection and thermal radiation. Thus, convection and radiation appear to accelerate thermal propagation. The cell, B22#, behaved differently, attributed to the lack of a heater in module B which meant that runaway was triggered via thermal propagation from other modules. When the temperature curve fell, sudden changes were observed, induced by the thermal runaway of nearby cells. Therefore, more details of the entire module at these key points are presented in Fig. 5.

In addition, it was observed that the average temperature curve in the no radiation (NR) model deviated more from the no convection (NC) and the full proposed models, especially for the last cells entering thermal runaway. This suggests that thermal radiation may have a significant effect on the thermal propagation characteristics, such as the occurrence time of thermal runaway, the peak temperature, and the time taken to reach the peak temperature. However, a comparison of only the first and last cells entering thermal runaway is insufficient to comprehensively assess the effects of natural convection and thermal radiation. Hence, the differences in the peak temperature and the time taken to reach the peak temperature were compared for the NC, NR, and TW models in all cells as these parameters are easy to acquire. As shown in Fig. 6, the maximum differences in cell temperature between the modules of the TW and NC models were seen for A14#, B41#, C1#, and D3#, with differences of −150 K, −97.2 K, −104.6 K, and −75.7 K, respectively. The maximum differences in the time taken to reach the peak were 20.3 s, 52.0 s, 14.5 s, and −16.2 s, corresponding to A10#, B31#, C22#, and D3#, respectively. These differences indicate that natural convection cannot be neglected in model development.

Similar comparisons were made between the temperature profiles of the TW and NR models to determine the effect of thermal radiation (Fig. 7). It was observed that the maximum differences in peak temperature in each module were −52.4 K, −43.9 K, −50.2 K,

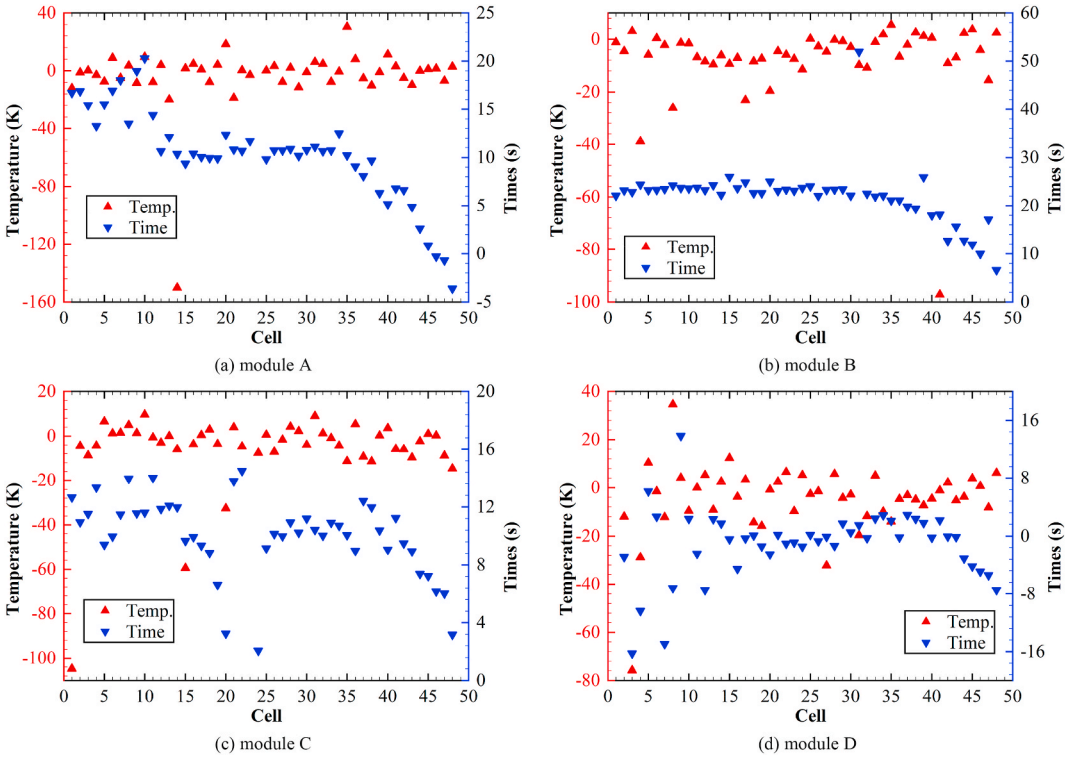

Fig. 6. Differences in the peak temperature and the time taken to reach the peak temperature for two different models: (a) module A, (b) module B, (c) module C, and (d) module D. Note: TW denotes the model proposed in the current work, and NC denotes the model without convection.

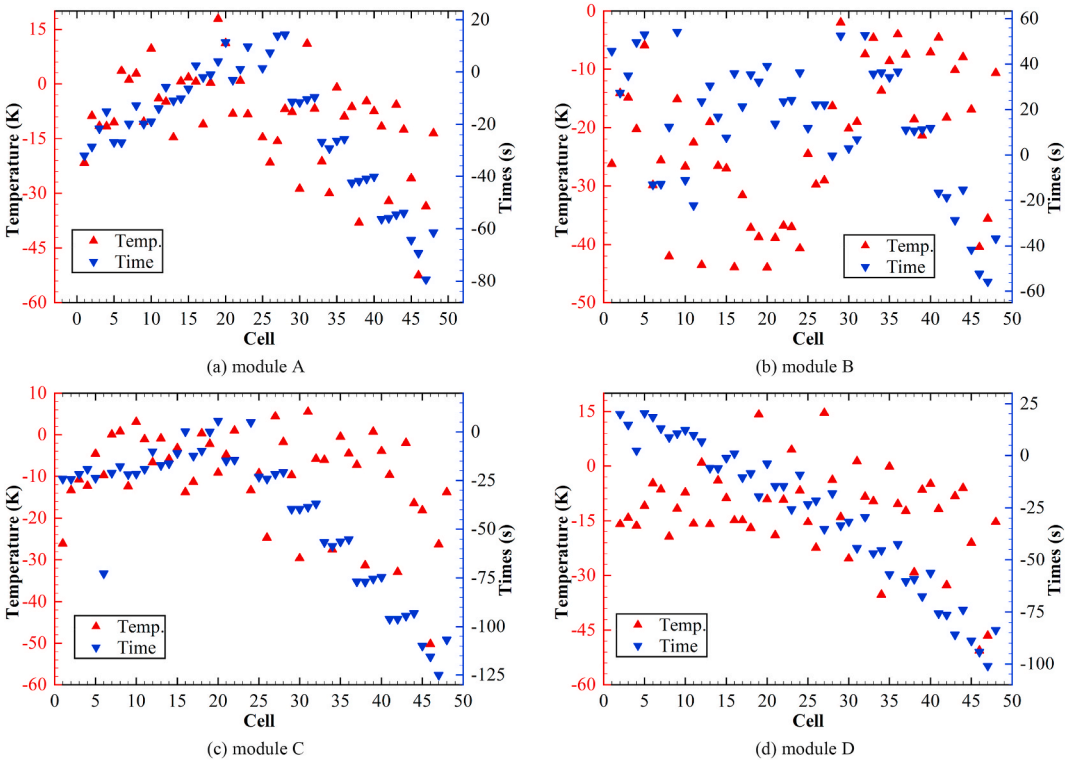

Fig. 7. Differences in the peak temperature and the time taken to reach the peak temperature for two different models: (a) module A, (b) module B, (c) module C, and (d) module D. Note: TW denotes the model proposed in the current work, and NR denotes the model without radiation.

and −50.6 K, which corresponded to A46#, B20#, C46#, and D46#, respectively. The maximum differences in the time taken to reach the peak temperature in each module were −79.4 s, −55.7 s, −125.0 s, and −101.0 s, corresponding to A47#, B47#, 47#C, D47#, respectively. These differences demonstrated the non-negligibility of thermal radiation in model development.

4.2. *Effect of the cell-to-cell gap*

To further explore the thermal propagation characteristics of thermal runaway at the pack level, four models were constructed from the framework of this work, considering cell-to-cell gaps of 1, 2, 3, and 4 mm. Unlike the earlier models discussed that had a gap width of 0 mm, the four models with greater gap widths reported the last cell to experience thermal runaway in each module to be 45#, compared with the previously reported 48#. This may be attributed to the higher aerial convection along the negative *y*-axis owing to gravitational effects. It is evident that the sequence in which cells enter thermal runaway is influenced by natural convection when the cell-to-cell gap is not bound to zero. The first cells entering thermal runaway in each module were A23#, B24#, C24#, and D2# for all models, with the exception of in that with a 1 mm cell-to-cell gap which reported B23# as the first in module B. Variations in the average temperatures of the cells in the models with a 1–4 mm cell-to-cell gap are depicted in Fig. 8. It is observed that the larger the gap, the larger the time interval until the last cell starts thermal runaway. This may be due to the increase in clearance and faster heat dissipation facilitated by the broader gap. Although there was no significant difference in the sequence of thermal runaway initiation within each module, the temperature drop rate of the cells following the temperature peak was significantly greater in the model with a 4 mm gap compared with that of the other models. Hence, although the larger gap increased the heat-transfer rate, there was no significant difference in the first cell to undergo thermal runaway due to the proximity of these cells to the heaters.

To better compare the temperature distribution for different gap widths, the distributions at different times in the four model simulations are depicted in Fig. 9. Given that the time lapsed before the last cells entered thermal runaway across the different models was between 1400 s and 1800 s, temperature distributions at 400 s, 800 s, 1200 s, and 1600 s were selected. From these results, it seems that the presence of a gap can mitigate the safety crisis by slowing the propagation of thermal runaway, allowing the driver more time to escape the vehicle. However, larger gaps result in smaller energy densities within the battery pack. Therefore, it is necessary to balance the cell-to-cell gap and energy density considerations in the design process.

5. Conclusions

In this study, a thermal abuse model based on the FEM was developed for a high-energy lithium-ion battery pack. The numerical model was coupled with thermal runaway ODEs, heat-transfer PDEs, natural convection in CFD, and thermal radiation computations. In addition, a methodology was proposed for a thermal abuse test utilizing multipoint heating. This method was found to be more

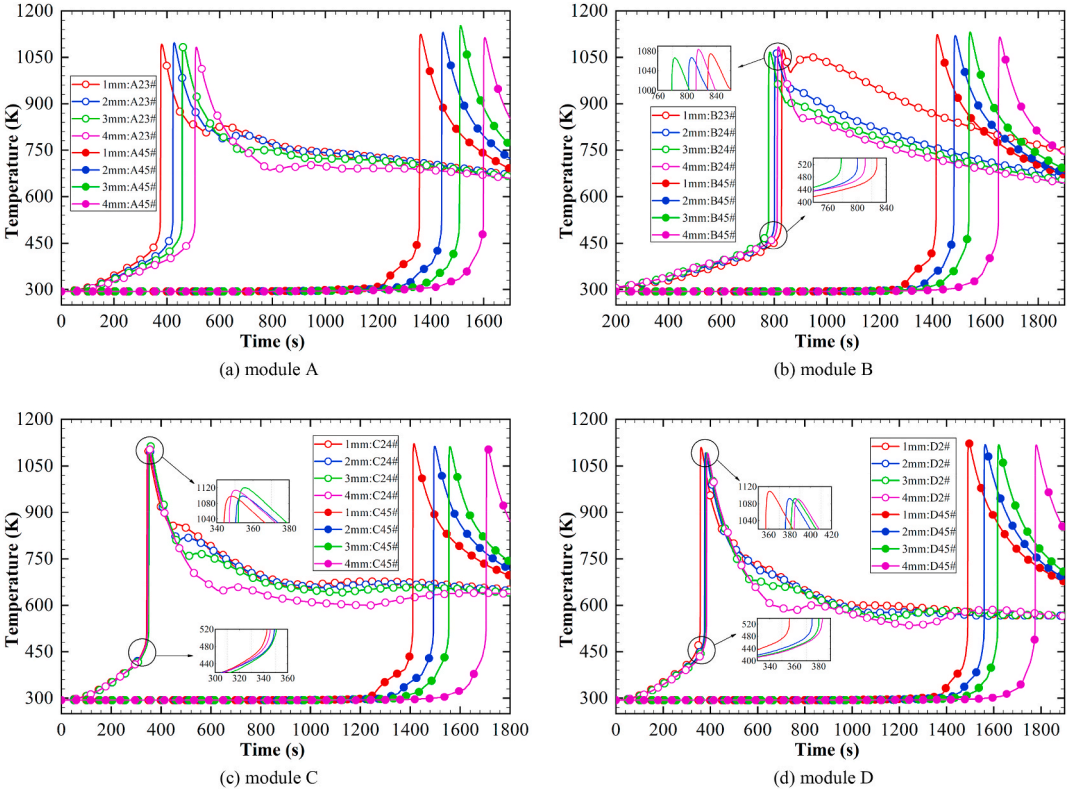

Fig. 8. Variations in the average temperatures of the cells in the models with 1–4 mm cell-to-cell gaps:(a) module A, (b) module B, (c) module C, (d) module D.

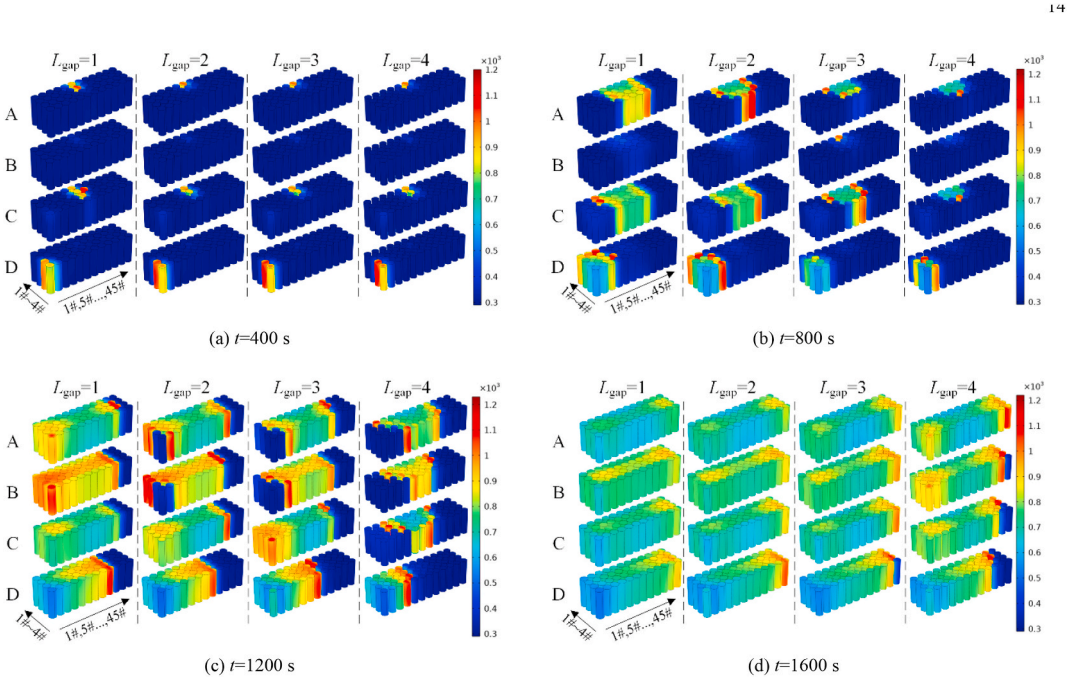

Fig. 9. Temperature distributions at selected time points in models with 1–4 mm cell-to-cell gaps: (a) t = 400 s, (b) t = 800 s, (c) t = 1200 s, (d) t = 1600 s.

consistent with real-world scenarios than single point heating. The proposed numerical model was simulated in its complete form (TW), as well as in two variations, one without natural convection (NC), and the other without thermal radiation (NR). The differences between the thermal propagation characteristics at the pack level for the three simulations were discussed. Natural convection and thermal radiation were observed to influence the time of occurrence of thermal runaway in cells, the peak temperature in each module, and the time taken to reach the peak temperature. The maximum differences between the TW and NC models for the peak temperature and the time taken to reach the peak temperature in all cells were −150 K and 52.0 s, respectively, while those between the TW and NR model were −52.4 K and −125.0 s. The results indicate that natural convection and thermal radiation play a vital role in the thermal propagation behavior predicted by the numerical modeling of thermal runaway. Furthermore, four additional models with cell-to-cell gaps of 1, 2, 3, and 4 mm were constructed to study the thermal propagation characteristics. The results showed that broader cell-to-cell gaps accelerated heat transfer, but compromised the energy density of the battery pack. Ultimately, the mathematical model developed in this study offers a significant contribution to the design of battery thermal management strategies to prevent thermal runaway at the pack level. However, this study has limitations, one of which is the random selection of heating points. Thus, in future work, we intend to determine the most unfavorable conditions for heating points at the pack level.

Author contributions

Yuanmao Li: Conceptualization, Methodology, Formal analysis, Software, Writing – original draft, Writing - review & editing. Guixiong Liu: Funding acquisition, Supervision, Data curation, Writing - original draft, Project administration. Zuyu Li: Software, Resources, Investigation, Visualization, Formal analysis, Writing - review & editing.

Declaration of competing interest

The authors declare that they have no known competing financial interests or personal relationships that could have appeared to influence the work reported in this paper.

Acknowledgements

This is a part research accomplishment of the Guangdong Key Areas R&D Project Power Battery System Testing and Evaluation Technology Research (2019B090908003).

References

[1] Y.-S. Duh, M.-T. Tsai, C.-S. Kao, Characterization on the thermal runaway of commercial 18650 lithium-ion batteries used in electric vehicle, J. Therm. Anal. Calorim. 127 (2016) 983–993, https://doi.org/10.1007/s10973-016-5767-1.
[2] H. Shen, Y. Zhang, Y. Wu, A comparative study on air transport safety of lithium-ion batteries with different SOCs, Appl. Therm. Eng. 179 (2020), https://doi.org/10.1016/j.applthermaleng.2020.115679.
[3] J. Lamb, L. Torres-Castro, J.C. Hewson, R.C. Shurtz, Y. Preger, Investigating the role of energy density in thermal runaway of lithium-ion batteries with accelerating rate calorimetry, J. Electrochem. Soc. 168 (2021), https://doi.org/10.1149/1945-7111/ac0699.
[4] H.U. Escobar-Hernandez, R.M. Gustafson, M.I. Papadaki, S. Sachdeva, M.S. Mannan, Thermal runaway in lithium-ion batteries: incidents, kinetics of the runaway and assessment of factors affecting its initiation, J. Electrochem. Soc. 163 (2016) A2691–A2701, https://doi.org/10.1149/2.0921613jes.
[5] R. Zhao, J. Liu, J. Gu, Simulation and experimental study on lithium ion battery short circuit, Appl. Energy 173 (2016) 29–39, https://doi.org/10.1016/j.apenergy.2016.04.016.
[6] D. Ren, X. Feng, L. Lu, M. Ouyang, S. Zheng, J. Li, X. He, An electrochemical-thermal coupled overcharge-to-thermal-runaway model for lithium ion battery, J. Power Sources 364 (2017) 328–340, https://doi.org/10.1016/j.jpowsour.2017.08.035.
[7] J. Allen, Review of polymers in the prevention of thermal runaway in lithium-ion batteries, Energy Rep. 6 (2020) 217–224, https://doi.org/10.1016/j.egyr.2020.03.027.
[8] B. Mao, H. Chen, Z. Cui, T. Wu, Q. Wang, Failure mechanism of the lithium ion battery during nail penetration, Int. J. Heat Mass Tran. 122 (2018) 1103–1115, https://doi.org/10.1016/j.ijheatmasstransfer.2018.02.036.
[9] C. Qi, Y. Zhu, F. Gao, K. Yang, Q. Jiao, Mathematical model for thermal behavior of lithium ion battery pack under overcharge, Int. J. Heat Mass Tran. 124 (2018) 552–563, https://doi.org/10.1016/j.ijheatmasstransfer.2018.03.100.
[10] C. Jin, Y. Sun, H. Wang, X. Lai, S. Wang, S. Chen, X. Rui, Y. Zheng, X. Feng, H. Wang, M. Ouyang, Model and experiments to investigate thermal runaway characterization of lithium-ion batteries induced by external heating method, J. Power Sources 504 (2021), https://doi.org/10.1016/j.jpowsour.2021.230065.
[11] J.K.S. Goodman, J.T. Miller, S. Kreuzer, J. Forman, S. Wi, J. Choi, B. Oh, K. White, Lithium-ion cell response to mechanical abuse: three-point bend, J. Energy Storage 28 (2020), https://doi.org/10.1016/j.est.2020.101244.
[12] S.T. Plunkett, C. Chen, R. Rojaee, P. Doherty, Y. Sik Oh, Y. Galazutdinova, M. Krishnamurthy, S. Al-Hallaj, Enhancing thermal safety in lithium-ion battery packs through parallel cell 'current dumping' mitigation, Appl. Energy 286 (2021), https://doi.org/10.1016/j.apenergy.2021.116495.
[13] D. Ouyang, M. Chen, R. Wei, Z. Wang, J. Wang, A study on the fire behaviors of 18650 battery and batteries pack under discharge, J. Therm. Anal. Calorim. 136 (2019) 1915–1926, https://doi.org/10.1007/s10973-018-7861-z.
[14] J. Xu, C. Lan, Y. Qiao, Y. Ma, Prevent thermal runaway of lithium-ion batteries with minichannel cooling, Appl. Therm. Eng. 110 (2017) 883–890, https://doi.org/10.1016/j.applthermaleng.2016.08.151.
[15] W. Chen, J. Jiang, J. Wen, Thermal runaway induced by dynamic overcharge of lithium-ion batteries under different environmental conditions, J. Therm. Anal. Calorim. 146 (2020) 855–863, https://doi.org/10.1007/s10973-020-10037-x.
[16] F. Larsson, B.-E. Mellander, Abuse by external heating, overcharge and short circuiting of commercial lithium-ion battery cells, J. Electrochem. Soc. 161 (2014), https://doi.org/10.1149/2.0311410jes. A1611–A1617.
[17] J. Xu, W. Mei, C. Zhao, Y. Liu, L. Zhang, Q. Wang, Study on thermal runaway mechanism of 1000 mAh lithium ion pouch cell during nail penetration, J. Therm. Anal. Calorim. 144 (2020) 273–284, https://doi.org/10.1007/s10973-020-10149-4.
[18] A. Börger, J. Mertens, H. Wenzl, Thermal runaway and thermal runaway propagation in batteries: what do we talk about? J. Energy Storage 24 (2019) https://doi.org/10.1016/j.est.2019.01.012.
[19] S. Abada, M. Petit, A. Lecocq, G. Marlair, V. Sauvant-Moynot, F. Huet, Combined experimental and modeling approaches of the thermal runaway of fresh and aged lithium-ion batteries, J. Power Sources 399 (2018) 264–273, https://doi.org/10.1016/j.jpowsour.2018.07.094.
[20] T. Cai, A.G. Stefanopoulou, J.B. Siegel, Modeling Li-ion battery temperature and expansion force during the early stages of thermal runaway triggered by internal shorts, J. Electrochem. Soc. 166 (2019) A2431–A2443, https://doi.org/10.1149/2.1561910jes.

[21] X. Feng, M. Ouyang, X. Liu, L. Lu, Y. Xia, X. He, Thermal runaway mechanism of lithium ion battery for electric vehicles: a review, Energy Storage Mater. 10 (2018) 246–267, https://doi.org/10.1016/j.ensm.2017.05.013.
[22] C.F. Lopez, J.A. Jeevarajan, P.P. Mukherjee, Characterization of lithium-ion battery thermal abuse behavior using experimental and computational analysis, J. Electrochem. Soc. 162 (2015) A2163–A2173, https://doi.org/10.1149/2.0751510jes.
[23] K. Shah, D. Chalise, A. Jain, Experimental and theoretical analysis of a method to predict thermal runaway in Li-ion cells, J. Power Sources 330 (2016) 167–174, https://doi.org/10.1016/j.jpowsour.2016.08.133.
[24] Z. Lei, Z. Maotao, X. Xiaoming, G. Junkui, Thermal runaway characteristics on NCM lithium-ion batteries triggered by local heating under different heat dissipation conditions, Appl. Therm. Eng. 159 (2019), https://doi.org/10.1016/j.applthermaleng.2019.113847.
[25] Z. An, K. Shah, L. Jia, Y. Ma, Modeling and analysis of thermal runaway in Li-ion cell, Appl. Therm. Eng. 160 (2019), https://doi.org/10.1016/j.applthermaleng.2019.113960.
[26] D.P. Kong, G.Q. Wang, P. Ping, J. Wen, Numerical investigation of thermal runaway behavior of lithium-ion batteries with different battery materials and heating conditions, Appl. Therm. Eng. 189 (2021). https://doi.org/10.1016/j.applthermaleng.2021.116661.
[27] R.M. Spotnitz, J. Weaver, G. Yeduvaka, D.H. Doughty, E.P. Roth, Simulation of abuse tolerance of lithium-ion battery packs, J. Power Sources 163 (2007) 1080–1086, https://doi.org/10.1016/j.jpowsour.2006.10.013.
[28] S. Wilke, B. Schweitzer, S. Khateeb, S. Al-Hallaj, Preventing thermal runaway propagation in lithium ion battery packs using a phase change composite material: an experimental study, J. Power Sources 340 (2017) 51–59, https://doi.org/10.1016/j.jpowsour.2016.11.018.
[29] H. Bian, Z. Wang, J. Jiang, Y. Yang, H. Wang, S. Chen, Thermal runaway hazard characteristics and influencing factors of Li-ion battery packs under high-rate charge condition, Fire Mater. 44 (2020) 189–201, https://doi.org/10.1002/fam.2783.
[30] T. Dong, P. Peng, F.M. Jiang, Numerical modeling and analysis of the thermal behavior of NCM lithium-ion batteries subjected to very high C-rate discharge/charge operations, Int. J. Heat Mass Tran. 117 (2018) 261–272, https://doi.org/10.1016/j.ijheatmasstransfer.2017.10.024.
[31] T.D. Hatchard, D.D. MacNeil, A. Basu, J.R. Dahn, Thermal model of cylindrical and prismatic lithium-ion cells, J. Electrochem. Soc. 148 (2001), https://doi.org/10.1149/1.1377592.
[32] G.H. Kim, A. Pesaran, R. Spotnitz, A three-dimensional thermal abuse model for lithium-ion cells, J. Power Sources 170 (2007) 476–489, https://doi.org/10.1016/j.jpowsour.2007.04.018.
[33] N. Tanaka, W.G. Bessler, Numerical investigation of kinetic mechanism for runaway thermo-electrochemistry in lithium-ion cells, Solid State Ionics 262 (2014) 70–73, https://doi.org/10.1016/j.ssi.2013.10.009.
[34] S. Santhanagopalan, Q.Z. Guo, P. Ramadass, R.E. White, Review of models for predicting the cycling performance of lithium ion batteries, J. Power Sources 156 (2006) 620–628, https://doi.org/10.1016/j.jpowsour.2005.05.070.
[35] K.S. Gavritchev, G.A. Sharpataya, A.A. Smagin, E.N. Malyi, V.A. Matyukha, Calorimetric study of thermal decomposition of lithium hexafluorophosphate, J. Therm. Anal. Calorim. 73 (2003) 71–83, https://doi.org/10.1023/A:1025125306291.
[36] T.G. Zavalis, M. Behm, G. Lindbergh, Investigation of short-circuit scenarios in a lithium-ion battery cell, J. Electrochem. Soc. 159 (2012) A848, https://doi.org/10.1149/2.096206jes. –A859.
[37] G. Guo, B. Long, B. Cheng, S. Zhou, P. Xu, B. Cao, Three-dimensional thermal finite element modeling of lithium-ion battery in thermal abuse application, J. Power Sources 195 (2010) 2393–2398, https://doi.org/10.1016/j.jpowsour.2009.10.090.
[38] P.J. Bugryniec, J.N. Davidson, S.F. Brown, Computational modelling of thermal runaway propagation potential in lithium iron phosphate battery packs, Energy Rep. 6 (2020) 189–197, https://doi.org/10.1016/j.egyr.2020.03.024.
[39] R.G. Belliveau, S.A. DeJong, N.D. Boltin, Z. Lu, B.M. Cassidy, S.L. Morgan, M.L. Myrick, A study of the mid-infrared emissivity of dried blood on fabrics, Forensic Chem 19 (2020), 100238, https://doi.org/10.1016/j.forc.2020.100238.
[40] F.P. Incropera, D.P. DeWitt, Fundamentals of Heat and Mass Transfer, sixth ed., John Wiley & Sons, 1996 https://doi.org/10.1016/j.applthermaleng.2011.03.022.
[41] Z. Li, Z. Luo, L.-C. Zhang, C.-H. Wang, Topological design of pentamode lattice metamaterials using a ground structure method, Mater. Des. 202 (2021), 109523, https://doi.org/10.1016/j.matdes.2021.109523.
[42] Y.-S. Duh, J.-H. Theng, C.-C. Chen, C.-S. Kao, Comparative study on thermal runaway of commercial 14500, 18650 and 26650 LiFePO4 batteries used in electric vehicles, J. Energy Storage 31 (2020), https://doi.org/10.1016/j.est.2020.101580.
[43] Y.S. Duh, Y. Sun, X. Lin, J. Zheng, M. Wang, Y. Wang, X. Lin, X. Jiang, Z. Zheng, S. Zheng, G. Yu, Characterization on thermal runaway of commercial 18650 lithium-ion batteries used in electric vehicles: a review, J. Energy Storage 41 (2021), https://doi.org/10.1016/j.est.2021.102888.

Abbreviations

EV: electric vehicle
SEI: solid electrolyte interface
ODEs: ordinary differential equations
CFD: computational fluid dynamics
3D: three-dimensional
GB: guo biao
SAE: Society of Automotive Engineers
UL:: Underwriter Laboratories
IEC: International Electrotechnical Commission
SOC: state of charge